Electromagnetic-thermal modeling of high-temperature superconducting coils with homogenized method and different formulations: a benchmark

A. Dadhich[1*], F. Grilli[2], L. Denis[3], B. Vanderheyden[3], C. Geuzaine[3], F. Trillaud[4,5], D. Sotnikov[6], T. Salmi[7], G. Hajiri[5], K. Berger[5], T. Benkel[8], G. dos Santos[9,10], B. M. O. Santos[9], F. G. R. Martins[11], A. Hussain[1], E. Pardo[1]

[1]Institute of Electrical Engineering, Slovak Academy of Sciences, Bratislava, Slovakia
[2]Karlsruhe Institute of Technology, Karlsruhe, Germany
[3]Montefiore Institute, University of Liege, Liege, Belgium
[4]Instituto de Ingeniería, Universidad Nacional Autónoma de México, 04510 CDMX, México
[5]Université de Lorraine, GREEN, F-54000 Nancy, France
[6]Paul Scherrer Institute, Wurenlingen, Switzerland
[7]Tampere University, Tampere, Finland
[8]Atled Engineering, Oxford, UK
[9]Electrical Engineering Department, Rio de Janeiro State University, Rio de Janeiro, 20550-900, Rio de Janeiro, Brazil
[10]Electrical Engineering Program, Universidade Federal do Rio de Janeiro, 21941-853 Rio de Janeiro, Brazil
[11]Electrical Engineering Department, Fluminense Federal University, Niterói, 21941-853 Rio de Janeiro, Brazil
[*]Corresponding author, email: anang.dadhich@savba.sk

March 2023

Abstract. High-temperature superconducting coils are used in various large-scale applications, like rotating machines and high-field magnets. However, modeling these coils is a complicated and time-consuming process, especially due to the non-linearity of the current-voltage characteristics of the superconductors and the complex multiphysics involved. In this work, we used a fast homogenized method to model the coupled electromagnetic and electrothermal properties of racetrack and pancake coils for different applications. For this purpose, various formulations wielding homogenization methods are used and benchmarked with each other, as well as with models considering the detailed structure of the HTS tapes. We observe a very good agreement between different models (homogenized and detailed), and we discuss the pros and cons of the inclusion of insulating layers between the turns in homogenization. This work was performed under the collaboration of the COST action modeling teams and can be used as a review of the state-of-the-art superconductor modeling techniques, and a source for the development and benchmark of future numerical methods.

1. Introduction

High-temperature superconducting (HTS) coils play a pivotal role in a myriad of applications ranging from high field magnets [1, 2, 3, 4], rotating machines [5, 6, 7, 8], and magnetic resonance imaging (MRI) systems to fusion reactors and particle accelerators [9, 10, 11, 12], demonstrating their utility across various scientific and industrial domains. As demands for higher magnetic field strengths, improved energy efficiency, and enhanced stability continue to increase, the imperative to advance the design and optimization of HTS coils becomes ever more pressing.

As HTS conductors and magnets are expensive and complicated to build, it is required to put emphasis on the design phase, for which computer simulations are a cost effective way to gain understanding on the device behavior and aiding the HTS magnet (or coil) design. Furthermore, the performance of these coils hinges on being run in a stable thermal state. HTS tapes may generate high power losses under time varying currents. The heat generation, due to these power losses can threaten the thermal stability, leading to catastrophic quench events that compromise the operation of such systems and potentially cause damage [13, 14, 15, 16, 17]. Therefore, understanding and optimizing heat management is paramount to unlock the full potential of the technology. Electromagnetic-thermal modeling is a crucial tool for understanding the intricate interplay between electromagnetic and thermal phenomena within superconducting coils. For a detailed multiphysics analysis of the superconducting coils, it is important to couple both electromagnetic and electrothermal modeling methods [18]. By accurately simulating the distribution of electrical currents, heat dissipation, and associated coupled thermal effects, these models provide invaluable insights into the performance characteristics and operational limits of superconducting systems.

Also, modeling HTS coils is a complicated and time-consuming process due to the inherent non-linear behavior of superconductors. One typical approach is to use detailed geometries of the HTS tapes, specially for REBCO tapes, which include specifying the geometry of all the layers involved explicitly, such as silver, hastelloy, stycast (between layers), copper, etc. Although it gives highly accurate results for superconductor multiphysics modeling (and cases like quench) [13, 19, 20], the main issue with this approach is the high computation times given the large number of degrees of freedoms to solve for. An alternative modeling approach is to use homogenized geometries, where all the layers of HTS tapes are considered as a single material with homogenized electromagnetic and thermal properties of involved materials [21, 20]. This reduces the computation times for the electrothermal calculations and quench phenomenon, as compared to the detailed model, while giving precise results, as we show in our results.

In this paper, we aim to delineate the state-of-the-art modeling techniques employed in studying the electromagnetic-thermal behavior of superconducting coils under different operating conditions using a homogenized method. We show the comparison between the detailed method and the homogenized method, as well as a comparison

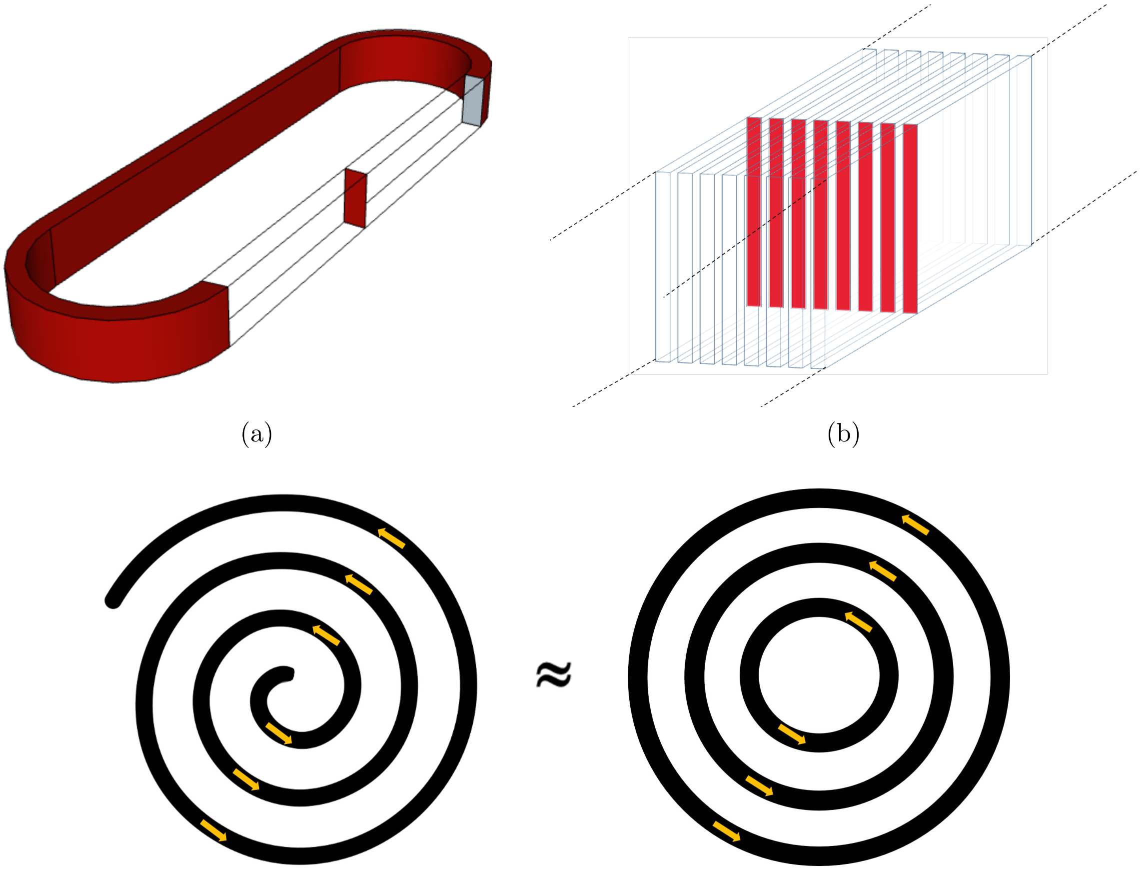

(a) (b)

(c)

Figure 1: (a) Racetrack coil geometry and (b) its cross-section. We use 5 tapes for the results in this paper. (c) The axisymmetric assumption for the pancake coil geometry.

between different electromagnetic-thermal models and their combinations for this type of approach. These models use a variety of schemes, such as Finite Element Method (FEM), Equivalent lumped circuit or variational principles to analyze temperature and power losses in insulated HTS coils (using YBCO tapes) for certain current profiles. The results are focused on showing the temperature rise of the coils, with input currents over critical current, and predicting the quench onset for benchmarking the models. The paper also acts as a review and benchmark of different electromagnetic-thermal formulations currently employed and developed by multiple teams in the international superconducting community, partially under COST action, and their applications. Moreover, this work also provides source material for benchmarking new and upcoming coupled electromagnetic-thermal models for racetrack and pancake coils that may be developed by other researchers.

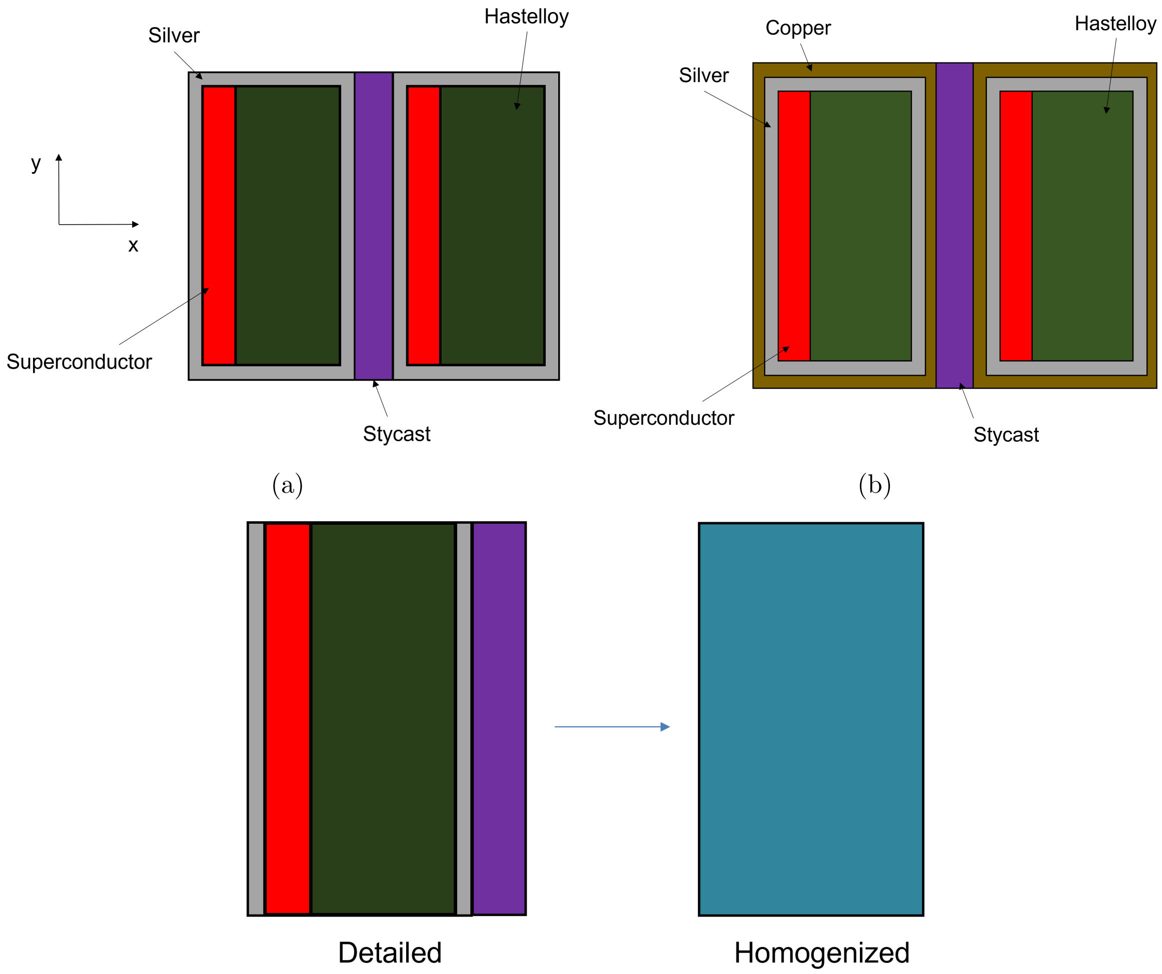

(a) (b)

(c)

Figure 2: Tape cross-section for the (a) racetrack coil and (b) pancake coil geometries. (c) Layer homogenization, which includes stycast. Homogenization for pancake coil tapes includes copper as well.

2. Modeling configurations

The work in this paper includes electromagnetic-thermal modeling for racetrack coil and pancake coil geometries. The input for the racetrack coil is an AC current with different peak current values at 5 Hz. The input for the pancake coil is a current ramp of $1\,\mathrm{A\,s^{-1}}$ for a duration of 180 s. These different current forms are chosen to simulate temperature rise in different common applications (i.e. racetrack coils in AC motors or wind turbines and pancake coils in high field magnets), and thus they differ in geometry and working conditions. These configurations are explained below.

2.1. Racetrack coil

We consider a racetrack coil composed of 5 turns arranged in series. The coil is assumed infinitely long, such that the curved parts are neglected and only its cross-section is modeled as shown in Figure 1 (a) and (b). The tape includes REBCO superconductor (HTS), silver (Ag), and hastelloy ($Hast$) layers. The turns are separated by an insulating stycast (sty) layer. Figure 2 shows the homogenization of these layers into a bulk, which includes stycast. The stycast inclusion in the homogenization reduces degrees of freedom, making models easier to develop, and we discuss the difference in results with and without stycast in homogenization in next sections. The top and bottom sections of silver layer are ignored in the homogenization, as they don't affect the results significantly due to their small aspect ratio with the conductor width.

The geometrical, electromagnetic, and thermal properties are shown in Table 1. The calculation of the homogenized properties is performed on the basis of [21] and the methodology shown in section 2.5. Their homogenized values are shown in Table 2.

2.2. Pancake coil

We consider a spiral pancake coil of 5 turns under the axisymmetric assumption, as shown in Figure 1 (c). The input of a fast current ramp makes this a more strenuous problem for the pancake as compared to the racetrack coil. The tapes have the same configuration as in the racetrack coil geometry, except that an additional copper layer is considered in this configuration (Figure 2 (b)). The reason for this inclusion is the extremely fast rise in temperature, due to the current ramp, in the case of pancake coil during quench, and copper helps in the thermal stability of the system, because of its higher diffusivity compared to other layers. From modeling perspective, as shown in [22], copper has low thermal capacity (or high diffusivity) at low temperatures as compared to the other layers (below 20 K),, which requires many timesteps to model this behavior, but at 77 K, copper is less burdening on models. The homogenization method of layers is the same as for the racetrack coil geometry, but with the inclusion of an additional copper layer, and its properties are considered in the calculation for homogenized values as shown in Tables 1 and 2.

2.3. Modeling parameters

The considered material properties are gathered in Tables 1 and 2. The properties are assumed constant at 77 K for the purpose of simplicity in benchmarking models, although all the models are able to consider the complete critical current density, $J_c(\mathbf{B}, T, \alpha)$, dependence, where $\mathbf{B}$, T, and α are the magnetic flux density, temperature, and magnetic field angle relative to the superconductor width, respectively. In general, J_c and n (power law exponent) depend on the magnetic flux density, $\mathbf{B}$, and temperature, T. In this work, we assume that J_c depends only on T, as shown later. Considering $J_c(\mathbf{B}, \alpha)$ dependence of REBCO, as well as the other dependencies of the layers

Table 1: Material properties.

Material	Thickness [µm]	k [$\mathrm{W\,m^{-1}\,K^{-1}}$]	C_p [$\mathrm{J\,kg^{-1}\,K^{-1}}$]	ρ [$\Omega\,\mathrm{m}$]	ρ_m [$\mathrm{kg\,m^{-3}}$]
HTS	2	9	156.65	3×10^{-7}	6390
Silver	2	400	235	1×10^{-8}	10500
Hastelloy	100	7	425	1.2×10^{-6}	8940
Stycast	50	0.8	138.6	1×10^{13}	2290
Copper	10	489.56	195.98	2.288×10^{-9}	8960

Table 2: List of parameters for racetrack (RT) and pancake (PC) coil geometries.

Quantity	Value	Homogenized quantities	Hom. value (RT)	Hom. value (PC)
Tape width [mm]	4	d_T [µm]	156	176
J_c (77 K) [$\mathrm{A\,m^{-2}}$]	1.875×10^{10}	$C_{p,hom}$ [$\mathrm{J\,kg^{-1}\,K^{-1}}$]	383.43	356.39
E_c [$\mathrm{V\,m^{-1}}$]	1×10^{-4}	$C_{v,hom}$ [$\mathrm{J\,m^{-3}\,K^{-1}}$]	2.6134×10^{6}	2.5159×10^{6}
Frequency [Hz]	5	k_x [$\mathrm{W\,m^{-1}\,K^{-1}}$]	2.0255	2.284
n [-]	30	k_y [$\mathrm{W\,m^{-1}\,K^{-1}}$]	15.1154	69.03
T_c [K] at 150 A	92	ρ_f [$\Omega\,\mathrm{m}$] ($T > T_c$)	3.18367	1.907
I_c [A]	150			

(like $n(T)$, thermal conductivity ($k(T)$), thermal capacity ($C_p(T)$), and so on) will mainly initiate quench earlier than the results shown [22], but the agreement (good or not) between the models should stay the same. However, for comparisons with experiments, and analyzing the quench (we just look at the onset of quench now), all these dependencies are required and will be included in the future as the models are developed further, given their specific applications in upcoming projects.

The coils are cooled using liquid nitrogen at 77 K, as shown in Figure 3 (a), with direct contact with coolant. The inner radius is kept at adiabatic conditions (no direct heat exchange with the coolant), due to the supposed existence of additional materials there in real systems, such as mechanical support structures. In reality, there may still be some cooling from the inner radius, either through thermal conduction with the support structure or direct contact with liquid nitrogen, depending on the system's configuration, and we just model a slightly extreme case. The cooling considers the complete convection coefficient (h) curve as shown in Figure 3 (b), which includes both nucleate boiling and film boiling [23].

2.4. Electric properties of the superconductor

The electric field power law relation holds inside the superconducting layer when the temperature is below the critical temperature, T_c:

$$\mathbf{E}(\mathbf{J}_{sc}) = E_c \left(\frac{|\mathbf{J}_{sc}|}{J_c} \right)^n \frac{\mathbf{J}_{sc}}{|\mathbf{J}_{sc}|}. \tag{1}$$

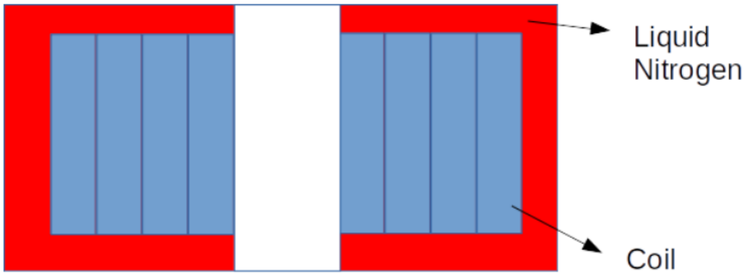

(a)

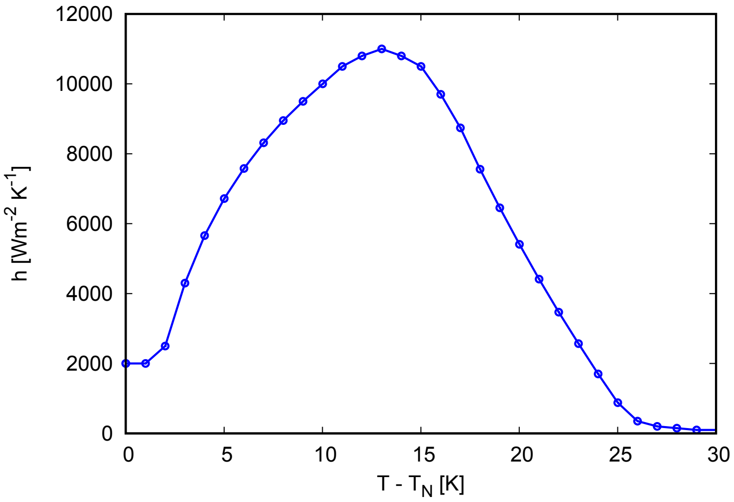

(b)

Figure 3: (a) Cooling configuration of the coils through liquid nitrogen and (b) convection coefficient curve considering liquid nitrogen cooling [23].

In the equation above, $\mathbf{E}$, $\mathbf{J}_{sc}$, and E_c are electric field, current density of the superconductor, and critical electric field, respectively. Naturally, if we consider a detailed model, where all layers are taken into account, $\mathbf{J} = \mathbf{J}_{sc}$ in the superconductor. From (1), we get the electrical resistivity (ρ_{sc}) in the superconducting region as

$$\rho_{sc}(\mathbf{J}_{sc}) = \left(\frac{E_c}{J_c}\right)\left(\frac{|\mathbf{J}_{sc}|}{J_c}\right)^{n-1}. \tag{2}$$

From 77 K to the critical temperature, T_c, we can assume

$$J_c(T) = J_{c,N}\frac{T_c - T}{T_c - T_N}, \tag{3}$$

where, T_N is the liquid nitrogen temperature, 77 K, and $J_{c,N}$ is J_c at that temperature. Naturally, $J_c = 0$ for $T > T_c$.

2.5. Homogenization

In this paper, we introduce a homogeneous model for superconducting tapes, instead of their complex detailed structure. While maintaining the fundamental characteristics of the tape, we observe fast computation because all constitutive elements are viewed as electrically coupled in parallel. In the results, we show that homogenization does not introduce significant errors compared to the detailed description. The homogenization of electrical properties can be performed as shown below [21].

First, we calculate the homogenized resistivity, ρ_f. For this, we consider electrical conductivity in parallel for both superconducting and normal regions.

The effective electrical conductivity, σ_{hom}, for normal regions can be calculated as

$$\sigma_{hom} = \frac{1}{d_T}\left[\frac{1}{\rho_{HTS}}d_{HTS} + \frac{1}{\rho_{Ag}}d_{Ag} + \frac{1}{\rho_{Hast}}d_{Hast} + \frac{1}{\rho_{Sty}}d_{Sty}\right], \tag{4}$$

where, d_T stands for total homogenized thickness, which is the sum of all individual layer thicknesses. Here, d and ρ are the individual layer thicknesses and resistivities, as shown in Table 1, where ρ_{HTS} is the normal state resistivity of the superconductor mentioned in the table. Depending on the model, d_T may or may not include Stycast thickness in it.

In order to take the superconductor into account, we assume that almost all the current flows in the superconducting layer. Then, $\mathbf{J}_{sc} \approx \mathbf{J}d_T/d_{HTS}$, where $\mathbf{J}$ is the current density of the homogenized material. This approximation is valid when $|\mathbf{J}|$ is much smaller than the critical engineering current density $J_{ce} \equiv J_c d_{HTS}/d_T$. Thus, the power law becomes

$$\mathbf{E}(\mathbf{J}) = E_c\left(\frac{|\mathbf{J}|}{J_{ce}}\right)^n \frac{\mathbf{J}}{|\mathbf{J}|}, \tag{5}$$

and

$$\rho_{sc}(\mathbf{J}) = \left(\frac{E_c}{J_{ce}}\right)\left(\frac{|\mathbf{J}|}{J_{ce}}\right)^{n-1}, \tag{6}$$

$$\sigma_{sc}(\mathbf{J}) = \frac{1}{\rho_{sc}(\mathbf{J})}. \tag{7}$$

Then, the effective resistivity of the homogenized material, ρ_f, can be calculated through parallel association, depending on the critical temperature (T_c), as,

$$\rho_f(\mathbf{J}) = \begin{cases} \frac{1}{\sigma_{sc}(\mathbf{J})+\sigma_{hom}} & \text{if } T < T_c, \text{and} \\ \frac{1}{\sigma_{hom}} & \text{if } T \geq T_c\ . \end{cases} \tag{8}$$

Finally, $\mathbf{E}$ is simply given by

$$\mathbf{E} = \rho_f(\mathbf{J})\mathbf{J}. \tag{9}$$

We assume a homogeneous model for the thermal properties of the superconducting tapes as well, where the thermal properties are homogenized as explained in [21]. The homogenized heat capacity per unit volume ($C_{v,hom}$) is

$$C_{v,hom} = \frac{1}{S}\int_S C_v dS, \tag{10}$$

where, C_v is heat capacity per unit volume of each material ($C_v \equiv C_p\rho_m$; ρ_m is the mass density; C_p is heat capacity at constant pressure), and the integral is done at the object cross-section S with cross-section differential ds. For our layered structure, the above equation turns into

$$C_{v,hom} = \frac{d_{HTS}C_{v,HTS} + d_{Ag}C_{v,Ag} + d_{hast}C_{v,hast} + d_{sty}C_{v,sty}}{d_T}. \tag{11}$$

If the model requires the homogenized specific heat capacity at constant pressure as input ($C_{p,hom}$), this is

$$C_{p,hom} = \frac{C_{v,hom}}{\rho_{m,hom}}, \tag{12}$$

where the homogenized mass density is

$$\rho_{m,hom} = \frac{d_{HTS}\rho_{m,HTS} + d_{Ag}\rho_{m,Ag} + d_{hast}\rho_{m,hast} + d_{sty}\rho_{m,sty}}{d_T}. \tag{13}$$

Lastly, we consider anisotropic thermal conductivities as

$$k_x = \frac{d_T}{\left(\frac{d_{HTS}}{k_{HTS}} + \frac{d_{Ag}}{k_{Ag}} + \frac{d_{hast}}{k_{hast}} + \frac{d_{sty}}{k_{sty}}\right)} \tag{14}$$

and

$$k_y = \frac{d_{HTS} \cdot k_{HTS} + d_{Ag} \cdot k_{Ag} + d_{hast} \cdot k_{hast} + d_{sty} \cdot k_{sty}}{d_T}, \tag{15}$$

where, k_x and k_y are the thermal conductivities in the x and y directions respectively (see Figure 2). In the x direction, the heat resistances of each layer are in series, while the heat resistances in the y direction are in parallel. For the pancake coil, which presents axial symmetry, we should replace k_x by k_r and k_y by k_z.

3. Modeling methods

3.1. Electromagnetic-thermal coupling

The coupling between electromagnetic and thermal physics appears both through [21]:

- the electric heat dissipation term, $p = \rho_r(\mathbf{J})|\mathbf{J}|^2$, which is computed from the electromagnetic problem ($p = \mathbf{E} \cdot \mathbf{J}$), and acts as a source term in the thermal problem;
- the corresponding temperature rise, which modifies the material properties of the electromagnetic problem. In this study, only the $J_c(T)$ dependence eq (3) of the superconducting layer is considered. All other material properties are considered constant with respect to temperature, for benchmark purposes, as discussed above.

The coupling of different electromagnetic and thermal formulations, as described in sections 3.2 and 3.3, is done in following combinations:

- **H** + FEM : For racetrack and pancake coils (Homogenized method).
- **H-A** + FEM : For racetrack coil (Detailed and Homogenized methods).

- **H**-ϕ + FEM : For racetrack and pancake coils (Detailed and Homogenized methods). The racetrack coil results use GetDP and the pancake coil results use COMSOL for this combination.
- **J**-**A** + FEM : For racetrack coil (Homogenized method).
- MEMEP + FD : For racetrack and pancake coils (Homogenized method).
- MEMEP + METEP : For racetrack coil (Homogenized method).
- **T**-**A** + Equivalent lumped circuit : For racetrack coil (Homogenized method).

The above combinations were made on the basis of the individual preference of each team. However, any thermal formulation specified here can work with any electromagnetic formulation mentioned in this paper, provided proper communication between the different solvers is implemented. As an initial step during this collaboration, we performed independent benchmarks of thermal (constant power density) and electromagnetic models (constant critical current density), which showed excellent agreement, after which we moved on to their coupling. These independent benchmarks are not shown in the paper to focus on the final results after coupling, as discussed in section 4.

3.2. Electromagnetic Formulations

3.2.1. **H** *formulation*

The **H** formulation solves Faraday's equation written in terms of magnetic field (**H**):

$$\frac{\partial}{\partial t}\left(\mu\mathbf{H}\right) + \nabla \times \left(\rho_r \nabla \times \mathbf{H}\right) = 0, \tag{16}$$

where, μ and ρ_r are the magnetic permeability and electrical resistivity, respectively. In the superconducting domains, the resistivity is in general a function of the current density and it is often modeled as a power-law (see (5) and (6)). In the homogenized tapes considered in this work, it takes the form of ρ_f from equation (8).

Early examples of this formulation are found in [24, 25], but the relatively straightforward implementation in commercial finite-element software [26, 27] made this formulation very popular. A review of its possible use for different superconducting applications is presented in [28].

3.2.2. **H**-**A** *formulation*

The **H** formulation (16) is a powerful tool for solving electromagnetic problems in FEM related to superconductors. It enables accurate solutions for electromagnetic problems involving materials with nearly zero resistivity (superconductors). For normal conducting or magnetic materials, the **A** formulation (17) suffices, utilizing the electrical conductivity ($1/\rho_r$) as a coefficient in the equation.

$$\frac{1}{\rho_r}\frac{\partial \mathbf{A}}{\partial t} + \nabla \times \left(\mu^{-1}\nabla \times \mathbf{A}\right) = 0, \tag{17}$$

where, $\mathbf{A}$ is the magnetic vector potential and t is the time. Notice that the equation above assumes Weyl's gauge, and hence zero scalar potential so that $\mathbf{E} = -\partial \mathbf{A}/\partial t$ (see section 1.3.1.2 of [29]). An alternative approach to the pure $\mathbf{H}$ formulation involves using the $\mathbf{H}$ formulation for low-resistivity (or superconducting) current-carrying elements in the model, and the $\mathbf{A}$ formulation for insulating or normal conducting materials with very high resistivity [30]. This recommendation is based on optimizing degrees of freedom, particularly for large models. In the case of 2D problems, the pure $\mathbf{H}$ formulation introduces two components for the solver (H_x and H_y for 2D, or H_r and H_ϕ for 2D axisymmetric), which increases degrees of freedom and computational cost. Conversely, $\mathbf{A}$ has just one component for the 2D case: A_z (or A_ϕ for axisymmetric configurations).

3.2.3. $\mathbf{H}$-ϕ *formulation*

The $\mathbf{H}$-ϕ formulation relies on the discretization of $\mathbf{H}$ and the magnetic scalar potential, ϕ. Such formulations are expected to efficiently handle the non-linearity described by the power law [31] as discussed in [32]. It is based on Ampère's law in the conducting subdomain Ω_c, where $\nabla \times \mathbf{H} = \mathbf{J}$, with $\mathbf{J} \neq 0$ being the current density flowing in Ω_c. Conversely, in the complementary non-conducting domain Ω_c^C, no current can flow ($\mathbf{J} = 0$), and $\nabla \times \mathbf{H} = \mathbf{0}$. Hence, we can define a magnetic scalar potential so that $\mathbf{H} = -\nabla\phi$. This approach avoids the introduction of the spurious currents in the non-conducting domain which is necessary in the case of the pure $\mathbf{H}$ formulation [28]. The equation is the same for both $\mathbf{H}$ and $\mathbf{H}$-ϕ formulations and reads (in weak formulation):

$$(\partial_t(\mu\mathbf{H}), \mathbf{H}')_\Omega + (\rho_r\, \nabla \times \mathbf{H}, \nabla \times \mathbf{H}')_{\Omega_c} = 0, \tag{18}$$

with the test function $\mathbf{H}'$ being defined on the same function space as $\mathbf{H}$. Here, the notation $(\cdot,\cdot)_\Omega$ denotes the inner product over the domain Ω. Time integration of (18) is performed with the implicit Euler method with an adaptive time-stepping procedure. The resulting system is solved iteratively using a Newton-Raphson (NR) scheme as described in [33]. Source currents are imposed strongly with cohomology basis functions [34]. The mesh is built with Gmsh [35] that also provides the tool to construct the cohomology basis functions. The FE resolution is carried out in GetDP [36]. Both software are open-source. Examples and codes are available online [37] as part of the Life-HTS toolkit, while further implementation details can be found in [33]

Later in the text, a distinction is made between the detailed model and the homogenized models. For the former, all the layers within the different tapes are separately considered and discretized to compute the local current density distribution in all layers (metallic and superconducting layers). For the homogenized models, the tapes are considered as a bulk material with homogenized electrical and thermal properties. Two submodels are built, one that includes the insulation between tapes (stycast) in the homogenized model and one that separates the insulation from the homogenized model. The homogenized models (with and without stycast) are described in section 2. The equivalent resistivity of the bulk conductor has been detailed in section 2.5.

The **H**-ϕ formulation is also used to model the pancake benchmark, but using the commercial software COMSOL Multiphysics. Here the implementation of the formulation is facilitated by using already existing modules. The method is explained in detail in [38], with the models being available on the web[39].

Consequently, in the benchmark, the *Magnetic Field Formulation* (mfh) module is used to implement the **H**-formulation on the conductive domain, and the *Magnetic Fields, No Currents* (mfnc) module for the ϕ-formulation in the non-conducting domains. *Magnetic Scalar Potential Discontinuity* features are used to impose the current in the turns, using the thickness of the Stycast layers for the required thin cuts. Hence, in the electromagnetic formulations, the Stycast is always considered as a perfect electric insulation and is not included in the homogenized properties. However, the Stycast layer is included when specified, in the thermal homogenized tape properties.

3.2.4. **J**-**A** *formulation*

The **J**-**A** has, as state variables, **J** and **A**, where the former is applied solely to the superconducting regions and the latter for the whole simulation domain [40, 41]. Each one acts as a source term for the other, consisting on a closed loop. The fundamental equation for the vector potential is

$$\nabla \times \frac{1}{\mu} \nabla \times \mathbf{A} = \mathbf{J}. \tag{19}$$

The source term **J** in (19) is the superconducting current, which is calculated from the non-linear Ohm's Law of $\mathbf{E} = \rho_r(\mathbf{J})\mathbf{J}$ as follows. Using that $\mathbf{E} = -\partial\mathbf{A} - \nabla\varphi$ the fundamental equation for the current density is

$$\rho_r(\mathbf{J})\mathbf{J} = -\frac{\partial \mathbf{A}}{\partial t} - \nabla\varphi, \tag{20}$$

where, **A** is the source term of (20) and φ is the scalar potential. If using the Coulomb's gauge for **A**, which requires boundary conditions consistent with that gauge, φ is the electrostatic potential, or voltage (see section 1.3.1.2 of [29]). Then, the term $\nabla\varphi$ could be used to couple the superconducting domain to an external circuit [42] or to impose an electric field directly on the FEM model. The other way is imposing proper constraints to ensure the Kirchhoff's law [43]. By using both ways, the metallic layers and substrate can be modeled as lumped parameters (circuit modeling) and coupled to superconducting layer [44, 45].

Alternatively, we can use Weyl's gauge ($\varphi = 0$) for cases with closed current loops, such as magnetization problems or coils with current constraints and no wires crossing the boundary of the modelled region [41]. For infinitely long racetrack coils, it is necessary to model both half-sections of figure 3(a), so that the net current in the total cross-section vanishes.

For this work, the superconducting region is homogenized as described in Figure 2. The homogenization process for **J**-**A** is the same as the ones applied in the **H** and **H**-ϕ formulations [41, 46]. An equivalent critical current density is computed with the ratio of the superconducting domain volume to the total volume of the homogenized region. This current density is applied to the $\mathbf{E}-\mathbf{J}$ model.

The **J**-**A** formulation here is implemented in COMSOL Multiphysics with the **A**-formulation from the *Magnetic Fields* (mf) module and equation (20) with the *Coefficient Form PDE* mathematics module. Its coupling with thermal equations is done by means of the explanation presented in the section 3.3.3.

3.2.5. MEMEP formulation

The Minimum Electro-Magnetic Entropy Production (MEMEP) method is a variatonal method that uses **J** as state variable [47, 48, 49]. In particular, MEMEP solves the following fundamental equation of **J**

$$\rho_r(\mathbf{J})\mathbf{J} = -\frac{\partial \mathbf{A}[\mathbf{J}]}{\partial t} - \frac{\partial \mathbf{A}_a}{\partial t} - \nabla\varphi, \tag{21}$$

where $\mathbf{A}[\mathbf{J}]$ is the vector potential in Coulomb's gauge ($\nabla\cdot\mathbf{A} = 0$ and $|\mathbf{A}| \to 0$ at $|\mathbf{r}| \to \infty$), which in general 3D problems it is (see section 1.1.3 of [29])

$$\mathbf{A}[\mathbf{J}](\mathbf{r}) = \frac{\mu_0}{4\pi}\int_{\Omega_C} \mathrm{d}^3\mathbf{r}' \frac{\mathbf{J}(\mathbf{r}')}{|\mathbf{r}-\mathbf{r}'|}. \tag{22}$$

In (21), $\mathbf{A}_a$ is the applied vector potential in Coulomb's gauge and φ is the electrostatic potential. We can describe the homogenized problem when we replace the local resistivity, ρ_f, into the homogenized one, ρ_l, from (8). The main feature of MEMEP is that is solves (21) at a certain time t by minimizing the following functional, given a known solution of **J** at time $t-\Delta t$,

$$F[\Delta\mathbf{J}] = \int_{\Omega_C} \mathrm{d}^3\mathbf{r}\left(\frac{1}{2}\Delta\mathbf{J}\cdot\frac{\mathbf{A}[\Delta\mathbf{J}]}{\Delta t} + \Delta\mathbf{J}\cdot\frac{\Delta\mathbf{A}_a}{\Delta t} + U(\mathbf{J}) + \nabla\varphi\cdot\mathbf{J}\right) \tag{23}$$

with

$$U(\mathbf{J}) = \int_0^{\mathbf{J}} \mathrm{d}\mathbf{J}'\cdot\rho_r(\mathbf{J}')\mathbf{J}'. \tag{24}$$

Above, $\mathbf{J} = \mathbf{J}(t)$ and $\Delta\mathbf{J} \equiv \mathbf{J}(t) - \mathbf{J}(t-\Delta t)$. We can obtain **J** by minimizing this functional because (21) is its Euler equation and the minimum of the functional is unique [49]. For this reason, MEMEP is a variational method. MEMEP computes the whole time evolution with the initial condition of $\mathbf{J} = 0$ at $t = 0$.

For very long shapes (usually referred as "infinite" shapes), both **J** and **A** follow the z direction and their single component is J_z and A_z, respectively. In Coulomb's gauge, $A_z[J_z]$ is (see section 1.1.3 of [29])

$$A_z[J_z](\mathbf{r}_2) = -\frac{\mu_0}{2\pi}\int_{S_C} \mathrm{d}^2\mathbf{r}_2' J_z(\mathbf{r}_2')\ln|\mathbf{r}_2' - \mathbf{r}_2| + \frac{\mu_0}{2\pi} I_T \ln l, \tag{25}$$

where S_C is the object cross-section region, $\mathbf{r}_2$ is the position vector in the cross-section, I_T is the total current in the cross-section, and l is the object length. In case that the object is a full racetrack coil like in figure 3(a), I_T vanishes.

For shapes with axial symmetry, such as pancake coils, both $\mathbf{J}$ and $\mathbf{A}$ follow the angular direction; and hence they have a single component, J_θ and A_θ, in that direction. In this configuration, the vector potential in Coulomb's gauge is (see section 1.1.3.2 of [29])

$$A_\theta(r,z) = \int_{S_C} \mathrm{d}r'\mathrm{d}z' J_\theta(r',z') a_{\text{loop}}(r, z-z', r') \tag{26}$$

with

$$a_{\text{loop}}(r,z-z',r') = \frac{\mu_0}{\pi\kappa}\sqrt{\frac{r'}{r}}\left[\left(1-\frac{\kappa^2}{2}\right)K(\kappa) - E(\kappa)\right] \tag{27}$$

and

$$\kappa^2 = \frac{4rr'}{(r+r')^2+(z-z')^2}, \tag{28}$$

where a_{loop} is the vector potential that generates a circular loop per unit current; r and z are the radial and axial coordinates, respectively; and $K(\kappa)$ and $E(\kappa)$ are the elliptic integrals of the first and second kind, respectively.

For both of these mathematically 2D geometries, we can drop the term with $\nabla\varphi$ in the functional of (23) for current constraints (ideal input current source or magnetization problem), as long as our test functions in the minimization method respect the current constraints [47].

3.2.6. **T**-**A** *formulation*

The **T**-**A** formulation of Maxwell's equations is based on solving the current vector potential **T** exclusively in the superconducting domain, while **A** is solved in all domains [50, 51]. The magnetic flux density **B** is calculated throughout the domain from **A** using the formula $\mathbf{B} = \nabla\times\mathbf{A}$. Here, **J** is derived from **T** according to the formula $\mathbf{J} = \nabla\times\mathbf{T}$, taking into account the non- linearity of the superconductor resistivity. The electric field **E** is determined by the magnetic flux density in accordance with Faraday's law. The governing equations of the **T**-**A** formulation are

$$\nabla^2\mathbf{A} = -\mu\mathbf{J}, \tag{29}$$

and

$$\nabla\times\rho_r\nabla\times\mathbf{T} = -\frac{\partial\mathbf{B}}{\partial t}, \tag{30}$$

where in (29) we assumed Coulomb's gauge for **A**.

The original **T**-**A** formulation, often called "**T**-**A** Full", allows the superconducting tape to be considered infinitely thin, with regard to the very narrow thickness of the superconducting layer. However, the approach of the homogeneous **T**-**A** formulation is to calculate the current density in the whole tape represented by a unit cell, whose thickness corresponds to the thicknesses of the various materials present in the tape. In that case, the current density J_s imposed in a tape in the $\mathbf{A}$ formulation is scaled and defined as the ratio d_{HTS}/d_T multiplied by J_z, where J_z is the current density calculated by the $\mathbf{T}$ formulation [52]. When implementing the formulation in COMSOL, the $\mathbf{A}$ formulation is calculated using COMSOL's magnetic field (mf) module, while the current vector potential $\mathbf{T}$ is solved in COMSOL's partial differential equations (PDE) module.

3.3. Thermal Formulations

3.3.1. Equivalent lumped circuit model

The lumped parameter thermal model involves dividing each turn of the coil into a single block element with uniform and homogeneous properties. As shown in Figure 4, heat flow in the x and y directions of the coil is represented by two branches, each containing a pair of thermal resistances equal to half of the thermal resistance in the respective direction. The average temperature T_{avr} is defined by a resistance connecting the x and y axes to form an artificial node where the average temperature is calculated. T_{avr} is computed at a single node connected by thermal resistances in the x and y directions. The average temperature of the coil is determined by averaging the temperatures of all the turns. The expressions of thermal resistance, heat capacity, and losses are given in [53]. For cooling, a convection resistance is applied to the two y-axis boundaries of each turn, named R_{cx}, and a convection resistance is added to the outermost turn to account for its surface area in contact with the coolant, named R_{cy}. The expression for the convective thermal resistance is determined with the surface area of the tapes in contact with the liquid nitrogen and the convective exchange coefficient 'h' indicated in Figure 3 (b) [54].

3.3.2. Finite Difference Method

An explicit Finite Difference (FD) method is used to solve the following thermal diffusion equation

$$\rho_m C_p(T)\frac{\partial T}{\partial t} = \nabla \cdot (\mathbf{k}(T)\nabla(T)) + p(T), \tag{31}$$

where $\mathbf{k}$ and p, are the orthotropic thermal conductivity tensor and heat dissipation per unit volume, respectively.

For axi-symmetric shapes, such as pancake coils, the thermal diffusion equation with orthotropic (or diagonal) $\mathbf{k}$ becomes

$$\rho_m C_p(T)\frac{\partial T}{\partial t} = \frac{1}{r}\frac{\partial}{\partial r}\left(r \cdot k_r(T)\frac{\partial T}{\partial r}\right) + \frac{\partial}{\partial z}\left(k_z(T)\frac{\partial T}{\partial z}\right) + p(T), \tag{32}$$

where, r and z are the radial and axial coordinates, respectively.

When dividing into concentric rings with several layers in the axial direction, the

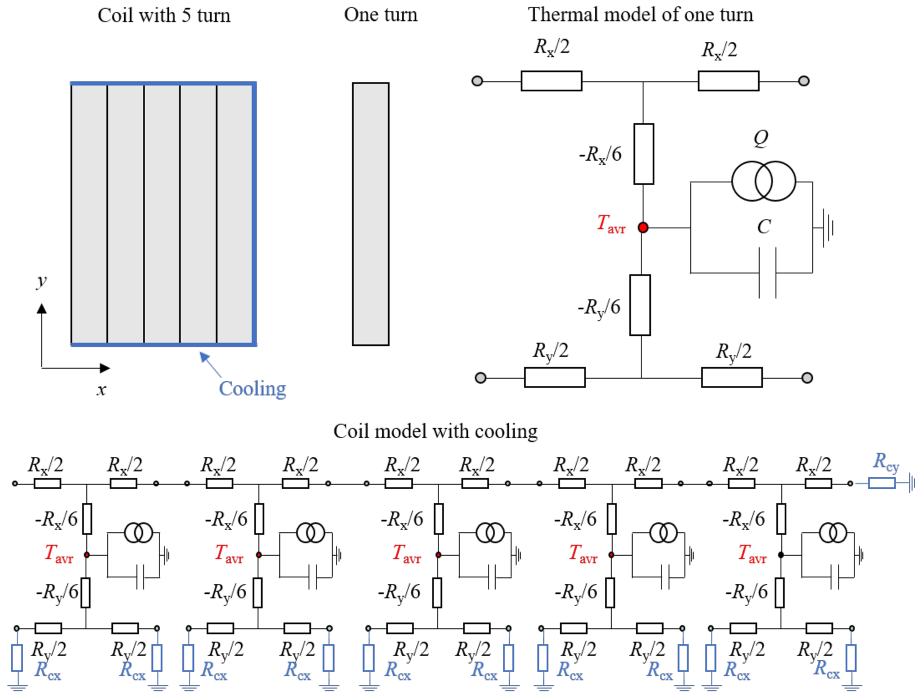

(a)

Figure 4: Diagram showing the discretization of the coil with the lumped parameter model including cooling.

thermal diffusion equation can be discretized as follows [22]

$$T_{ij}^{n+1} = T_{ij}^{n} + \frac{\Delta t^{n+1}}{C_{v,i,j}^{n}\Delta r_{i,j}} \left[\frac{r_{i+\frac{1}{2},j}}{r_{i,j}} k_{r,i+\frac{1}{2},j} \frac{T^n_{i+1,j}-T^n_{i,j}}{r_{i+1,j}-r_{ij}} - \frac{r_{i-\frac{1}{2},j}}{r_{i,j}} k_{r,i-\frac{1}{2},j}\frac{T^n_{i,j}-T^n_{i-1,j}}{r_{i,j}-r_{i-1,j}}\right] + \frac{\Delta t^{n+1}}{C^n_{v,i,j}\Delta z_{i,j}}\left[k_{z,i,j+\frac{1}{2}}\frac{T^n_{z,i,j+1}-T^n_{z,i,j}}{z_{i,j+1}-z_{i,j}} - k_{z,i,j-\frac{1}{2}}\frac{T^n_{z,i,j}-T^n_{z,i,j-1}}{z_{i,j}-z_{i,j-1}}\right] + \frac{\Delta t^{n+1}p^n_{i,j}}{C_{v,i,j}}, \tag{33}$$

where C_v is the heat capacity per unit volume at constant pressure ($C_v \equiv \rho_m C_p$); indices i and j identify the center of the cells in the r and z directions, respectively; and $i \pm 1/2$ and $j \pm 1/2$ label the surfaces in the r and z directions, respectively, of cell i, j. The super-index n labels the time step. This formalism is also valid for non-uniform mesh and variable time step, $\Delta t^{n+1} = t^{n+1} - t^n$. The equivalent heat conductivity at the cell surfaces are calculated from $k_r(T_{ij})$ and $k_z(T_{ij})$ as detailed in [22]. For the surfaces in contact with the liquid nitrogen, we also take the convection coefficient h into account.

For infinitely long problems like the racetrack coil in figure 3(b), the thermal diffusion equation with diagonal $\mathbf{k}$ is

$$\rho_m C_p(T)\frac{\partial T}{\partial t} = \frac{\partial}{\partial x}\left(k_x(T)\frac{\partial T}{\partial x}\right) + \frac{\partial}{\partial y}\left(k_y(T)\frac{\partial T}{\partial y}\right) + p(T). \tag{34}$$

Similarly, the general discretized form of equation (34) is

$$T_{i,j}^{n+1} = T_{i,j}^{n} + \frac{\Delta t^{n+1}}{C_{v,i,j}\Delta x_{i,j}}\left[k_{x,i+\frac{1}{2},j}\frac{(T_{i+1,j}^{n} - T_{i,j}^{n})}{x_{i+1,j} - x_{i,j}} - k_{x,i-\frac{1}{2},j}\frac{(T_{i,j}^{n} - T_{i-1,j}^{n})}{x_{i,j} - x_{i-1,j}}\right] + \frac{\Delta t^{n+1}}{C_{v,i,j}\Delta y_{i,j}}\left[k_{y,i,j+\frac{1}{2}}\frac{(T_{i,j+1}^{n} - T_{i,j}^{n})}{y_{i,j+1} - y_{i,j}} - k_{y,i,j-\frac{1}{2}}\frac{(T_{i,j}^{n} - T_{i,j-1}^{n})}{y_{i,j} - y_{i,j-1}}\right] + \frac{p_{i,j}\Delta t^{n+1}}{C_{v,i,j}}, \quad (35)$$

in rectangular coordinate system (x and y instead of r and z, respectively). For the purpose of the results shown in this paper, C_p and C_v correspond to $C_{p,hom}$ and $C_{v,hom}$ as defined in section 2.5.

In contrast to the implicit forms of FD method, which are unconditionally stable, explicit FD has the following stability conditions for pancake coil, which is dependent on the mesh size and thermal properties:

$$\Delta t \leq \frac{1}{2}\frac{\Delta r^2 \Delta z^2}{\Delta r^2 + \Delta z^2} \times \frac{\min(C_v)}{\max(k)}. \quad (36)$$

This stability condition is the same for the racetrack coil but using cartesian coordinates. The purpose of using explicit FD is its ease in development (particularly when implemented in in-house software) and fast computation times [22].

In this article, we couple FD with MEMEP by the following iterative method. First, we solve T by FD and update $J_c(T)$; then, we solve $\mathbf{J}$ by MEMEP and update p; and we repeat the process until the difference in the result of $\mathbf{J}$ and T between two iterations is below a certain tolerance.

3.3.3. Finite Element Method

The scalar temperature field T is approximated by nodal basis functions in the thermal domain of interest (Ω_T). The weak formulation of the thermal FE problem is based on the balance heat equation (31) yielding the following weak form:

$$\left(\rho_m C_p\, \partial_t T, T'\right)_{\Omega_T} + \left(\mathbf{k}\nabla(T), \nabla(T')\right)_{\Omega_T} + \langle \bar{f}(T), T'\rangle_{\Gamma_T} = \left(p, T'\right)_{\Omega_T}, \quad (37)$$

with T' denoting a test function and $\langle \cdot, \cdot \rangle_{\Gamma_T}$ denoting the inner product on the boundary surface Γ_T of the domain Ω_T. The boundary conditions (BCs) are taken into account via the function $\bar{f}(T)$. Adiabatic surfaces correspond to $\bar{f} = 0$, while convection is modeled with the convection coefficient h such that $\bar{f}(T) = h(T) \cdot (T - T_N)$ with T_N being the liquid nitrogen temperature (see section 2.3 and Figure 3).

The time-integration of (37) is performed with the implicit Euler scheme. In GetDP, the two-way coupling between the electromagnetic and the thermal subproblems is handled with staggered coupling, in which both subproblems are solved iteratively until convergence is reached. The coupling is implemented as part of the Life-HTS toolkit and the open-source codes are available online [37].

3.3.4. METEP formulation

The minimum Electro-Thermal Entropy Production (METEP) method solves the thermal diffusion equation (31) by a variational principle [21]. The thermal diffusion equation derives from the energy balance equation

$$p = \frac{\partial U_T(T(\mathbf{r},t))}{\partial t} + \nabla \cdot \mathbf{G}(\nabla T), \tag{38}$$

with

$$\mathbf{G}(\nabla T) = -\mathbf{k}\nabla T, \quad U_T(T) = \int_0^T \mathrm{d}T' C_v(T'), \tag{39}$$

where, $p = \mathbf{J} \cdot \rho_r(\mathbf{J})\mathbf{J}$ is the heat rate per unit volume, t is the time, $\mathbf{G}$ is the heat flux density, and $U_T(T)$ is the internal energy per unit volume at constant volume and assuming negligible thermal expansion. In time discretized form, equation (38) is

$$p = \frac{U_T(T(t)) - U_T(T(t-\Delta t))}{\Delta t} + \nabla \cdot \mathbf{G}(\nabla T). \tag{40}$$

We can construct a functional that its Euler equation is the equation above. Thus, we obtain T at time t by minimizing that functional and knowing the temperature at the previous time step $T_{\mathrm{prev}} \equiv T(t - \Delta t)$. This functional is [21]

$$F[T] = \int_{\Omega_T} \mathrm{d}^3\mathbf{r} \left\{ \Big(h_T(T) - U_T(T_{\mathrm{prev}})T \Big) \frac{1}{\Delta t} + \frac{1}{2} \nabla T \mathbf{k} \nabla T - q(\mathbf{J},\mathbf{B},T) \right\}, \tag{41}$$

with

$$\begin{aligned} h_T(T) &= \int_0^T \mathrm{d}T' U_T(T'), \\ q(\mathbf{J},\mathbf{B},T) &\equiv \int_0^T \mathrm{d}T' \mathbf{J} \cdot \rho_r(\mathbf{J},\mathbf{B},T')\mathbf{J}, \end{aligned} \tag{42}$$

where, Ω_T is the region where the temperature field is modelled and $\rho_r(\mathbf{J},\mathbf{B},T)$ is the material non-linear resistivity, which depends on the magnetic flux density and temperature. In superconductors, the $\mathbf{B}$ and T dependence appears mainly through $J_c(\mathbf{B},T)$.

In order to take a temperature-dependent $\mathbf{k}$ into account, we need to iterate at the same time step. That is, we solve the solution for a given $\mathbf{k}$, then we solve T, we update $\mathbf{k}$, and repeat the process until the change in T is below a certain tolerance. For the surfaces in contact with the liquid nitrogen, we consider an effective conductivity that contains the convection coefficient h [21].

In this work, we couple METEP with the electromagnetic MEMEP in the same way as we couple FD with MEMEP (section 3.3.2). For METEP, we need less iterations because the direct effect of temperature in the power dissipation is already taken into account in $q(\mathbf{J},\mathbf{B},T)$.

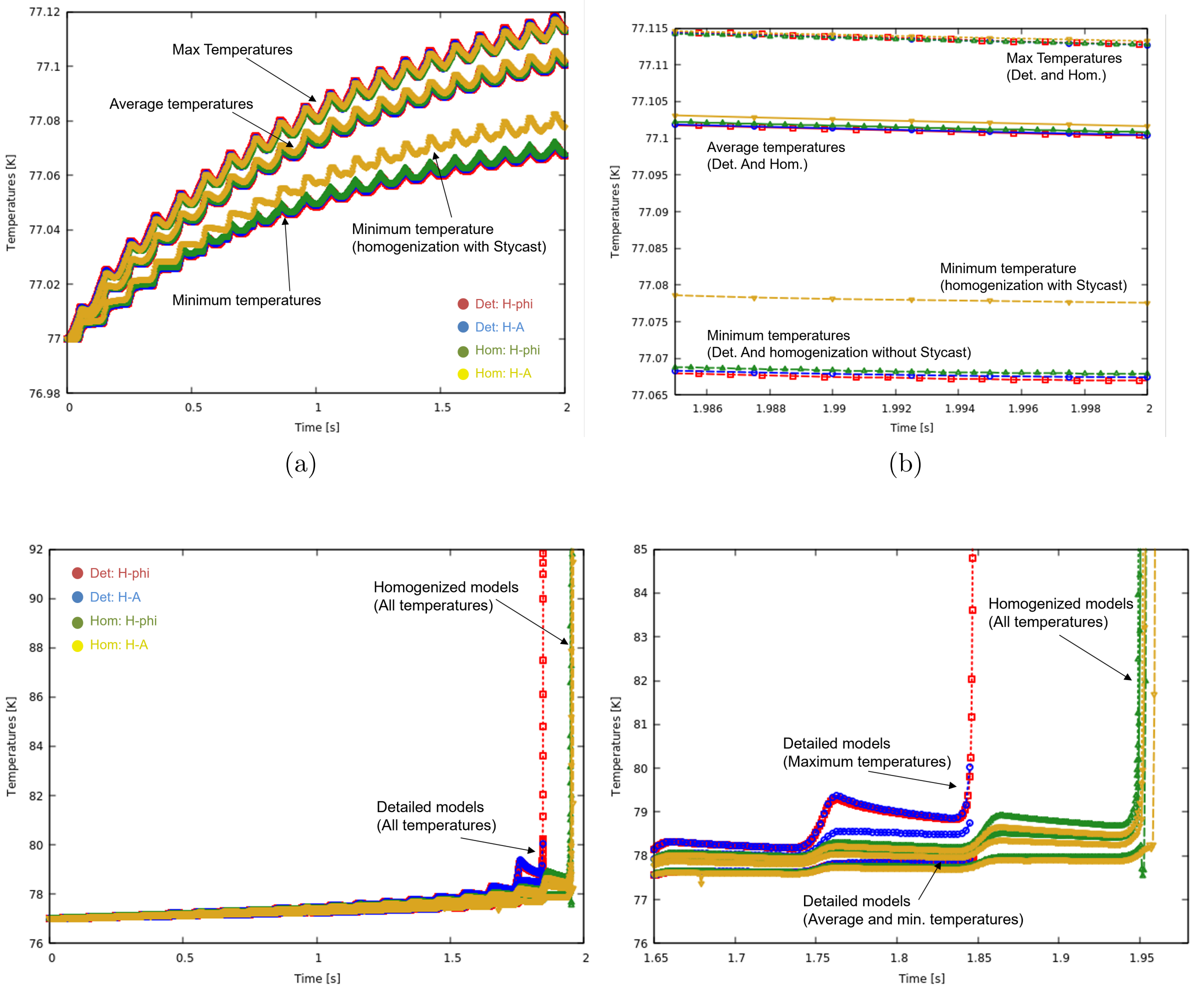

(a) (b)

(c) (d)

Figure 5: Comparison between detailed (Det.) and homogenization (Hom.) methods for racetrack coil in (a) 170 A and (c) 180 A with cooling. (b) and (d) are zoomed versions of (a) and (c) respectively. The homogenized models show good agreement with detailed models except for the minimum temperature at 170 A. It can be solved by keeping stycast out of homogenization.

4. Results and Discussion

4.1. Benchmark of homogenized method with detailed method: Racetrack coil

A comparison between detailed models and homogenized models is shown in Figure 5. For this specific comparison, **H-A** and $\mathbf{H}$-ϕ formulations have been employed. FEM is used in all these cases to solve coupled thermal properties. $\mathbf{H}$-ϕ + FEM models are solved with the GetDP software, whereas, **H-A** + FEM uses COMSOL for these calculations. Furthermore, homogenized $\mathbf{H}$-ϕ + FEM keeps the stycast layer out of the homogenization. Hence the thermal and electromagnetic properties of the insulating layer are considered separately. Here, the models consider cooling conditions as shown in Figure 3.

Firstly, we see in Figure 5 (a-d), that perfect agreement is obtained between detailed models for the maximum, minimum, and average temperatures. This confirms the validity of detailed models for different input currents (170 A and 180 A) and temperature rise until the onset of quench.

At low input current (170 A), which is comparatively higher than I_c (150 A at $T = T_N$), some temperature rise appears in the coil. Here, there is perfect agreement between detailed models and homogenized models for the maximum and average temperatures (Figure 5 (a,b)). However, a small difference in the minimum temperatures can be observed, as the complete homogenized model (H-with inclusion of Stycast) predicts slightly higher minimum temperature than others (detailed models, and homogenized model without stycast). One reason for this discrepancy can be the lower thermal conductivity of stycast (Table 1), which acts as a thermal insulating layer. Furthermore, the complete homogenized model cannot capture the local temperature fluctuations (largest temperature in REBCO layers due to heat dissipation and lowest temperature in stycast) across layers. Since the minimum temperature occurs at the stycast layer (particularly, at the outer radius in contact with liquid nitrogen), the fully homogenized model results in a higher minimum temperature because it averages the stycast with its neighbouring superconducting tape. In any case, the maximum and average temperatures are the most relevant quantities for quench analysis in applications. For these cases, stycast can be kept in the homogenization (even if they have high electrical resistivity compared to other layers), as it reduces the complexity of developing models and allows to reduce their computing times. It is especially relevant when dealing with real-life cases that may include hundreds of turns in a racetrack coil.

At higher input current (180 A), thermal runaway is seen at around 1.85 s for the detailed models and at 1.95 s for the homogenized models (Figure 5 (c,d)). As discussed above, the maximum temperature is the relevant quantity associated with a local quench (Figure 5 (d)). This difference in thermal runaway instants (almost half a cycle) can be attributed to minor differences in electromagnetic formulations (1-2 percent in temperature), as the local temperature within the REBCO layer is slightly underestimated by the homogenized model. Consequently, the corresponding local J_c is slightly overestimated, which in turn leads to an underestimated dissipated power density. These minor differences may build up as current cycles go by until the thermal runaway is triggered at different instants. However, the corresponding difference in quench prediction can also be only a particular model specific, as some homogenized models are able to predict quench onset like detailed model, as we see in the next section.

4.2. Benchmark of different homogenized models: Racetrack coil

The homogenized models using different combinations of coupled electromagnetic and thermal formulations (as described in section 3.1) are compared in this subsection.

The comparisons are performed for both adiabatic (no cooling with liquid nitrogen) and cooling conditions. Adiabatic results are important to see, as the coolant and h curves can vary for different applications, and adiabatic results show how the systems perform without the presence of any coolants. Additionally, the same mesh (1 element in thickness, 50 elements in width) and number of time steps (200 per cycle) are used for these calculations by different models and research teams for consistent comparison. In the following sections, this mesh is referred to as the *standard mesh*.

Firstly, the comparison between homogenized models can be seen in Figure 6 (a-f) for 170 A current input. The homogenized models show very good agreement in the average temperatures for both adiabatic and cooling conditions in these graphs. The homogenized models again show very good agreement with the detailed model (**H**-**A** + FEM), as can be seen in Figure 6 (c,d) and already observed in Figure 5 (a,b). Here, the homogenized **H**-**A** + FEM model shows a slight difference in the average temperature as compared to Figure 5 (a,b) due to lower mesh, whereas other models are closer to the detailed model with the standard mesh. Additionally, the combinations of MEMEP + FD and MEMEP + METEP show slightly higher temperature rise than other models for cooling conditions (Figure 6 (c,d)). This is due to comparatively higher power loss prediction by MEMEP (Figure 6 (f)). There are slight differences in power loss predictions between all models (Figure 6 (e,f)). However, these differences have only a minor impact as the temperature difference between all models is less than three significant figures after the decimal (Figure 6 (a-d)). Overall, these results show good agreement between all the considered models.

The 180 A input current (1.2 I_c at $T = T_N$) is an interesting case due to the current being high enough to initiate thermal runaway as opposed to the 170 A current case. For this input, the models have a good agreement for the adiabatic case (Figure 7 (a,b)), and quench is seen at 1.25 s (around the 6th cycle). Here, the **H** + FEM combination predicts quenching slightly earlier using the standard mesh, but improving the mesh for this combination brings the temperature curve (red dashed line- high mesh) closer to other models. This difference can be attributed to the numerical error in the mesh along with the slightly higher power generation with the **H** formulation. Similarly, for 180 A input with convection cooling conditions, there is good agreement between different models, although, some models predict quench half a cycle later (at 1.95 s) using the standard mesh (Figure 7 (c,d)). The same can be seen in the power loss results (Figure 7 (e)) by different models at these times, where there is a sudden jump in power at the time of thermal runaway with good agreement between different models. Interestingly, some homogenized models (like **H** +FEM and MEMEP + FD) show good agreement with the detailed model here, which is in contrast to the results in the previous section (Figure 5 (c,d)). We note here that these small differences in quench prediction times may be attributed to the minor differences in power loss calculations by different models, which can be as low as 1 percent. This small discrepancy, which is usually ignored during model comparisons, can make a big difference in quench predictions (by around half a cycle at least), as highlighted in Figure 8. As observed, thermal runaway occurs one

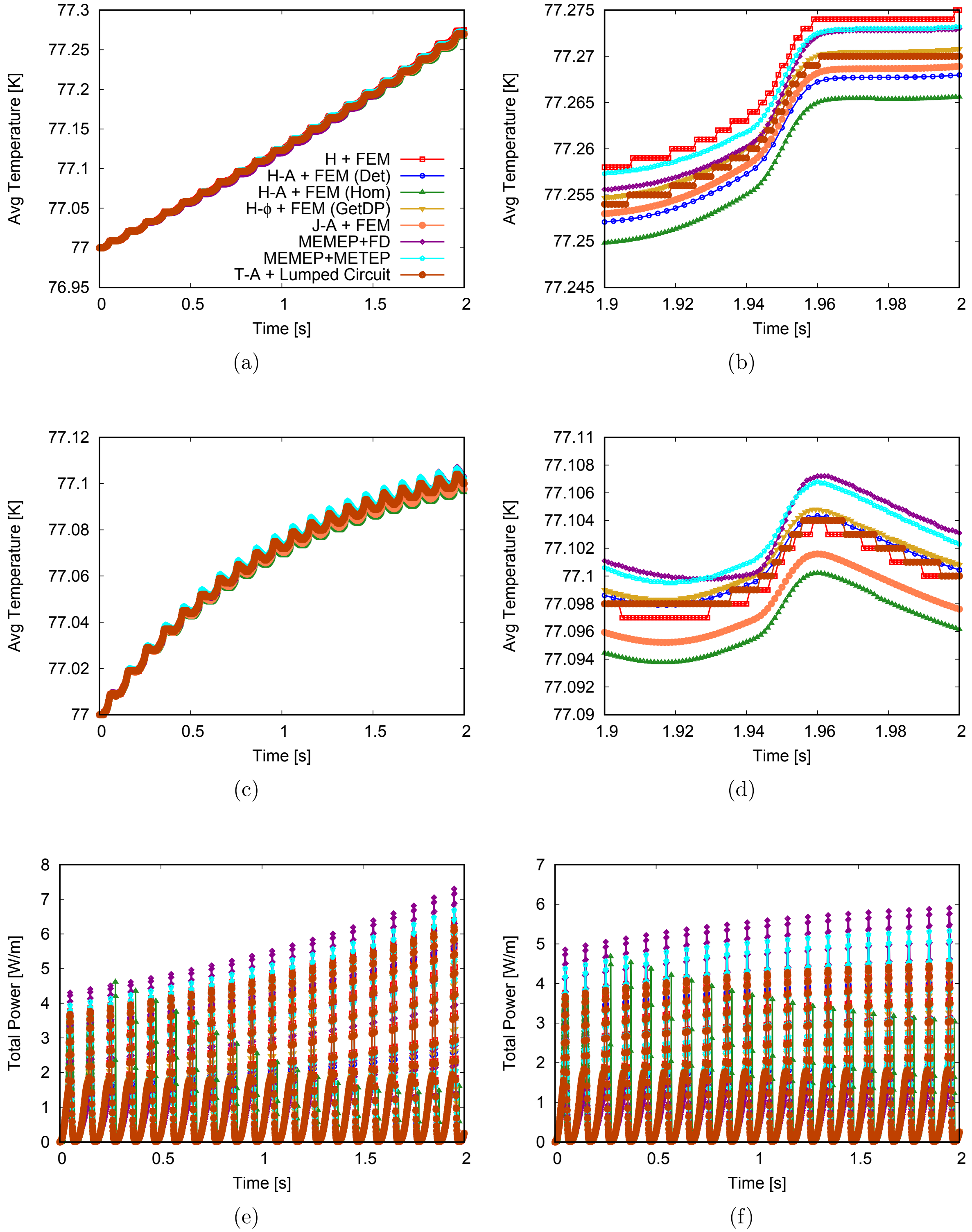

(a)

(b)

(c)

(d)

(e)

(f)

Figure 6: Comparison between homogenized models for racetrack coil at 170 A. Average temperatures are shown in (a) at adiabatic conditions, and in (c) with cooling conditions. (b,d) are zoomed versions of (a) and (b) respectively. The total power dissipation is shown in (e) and (f) at adiabatic and cooling conditions respectively. All figures use the same legend as (a).

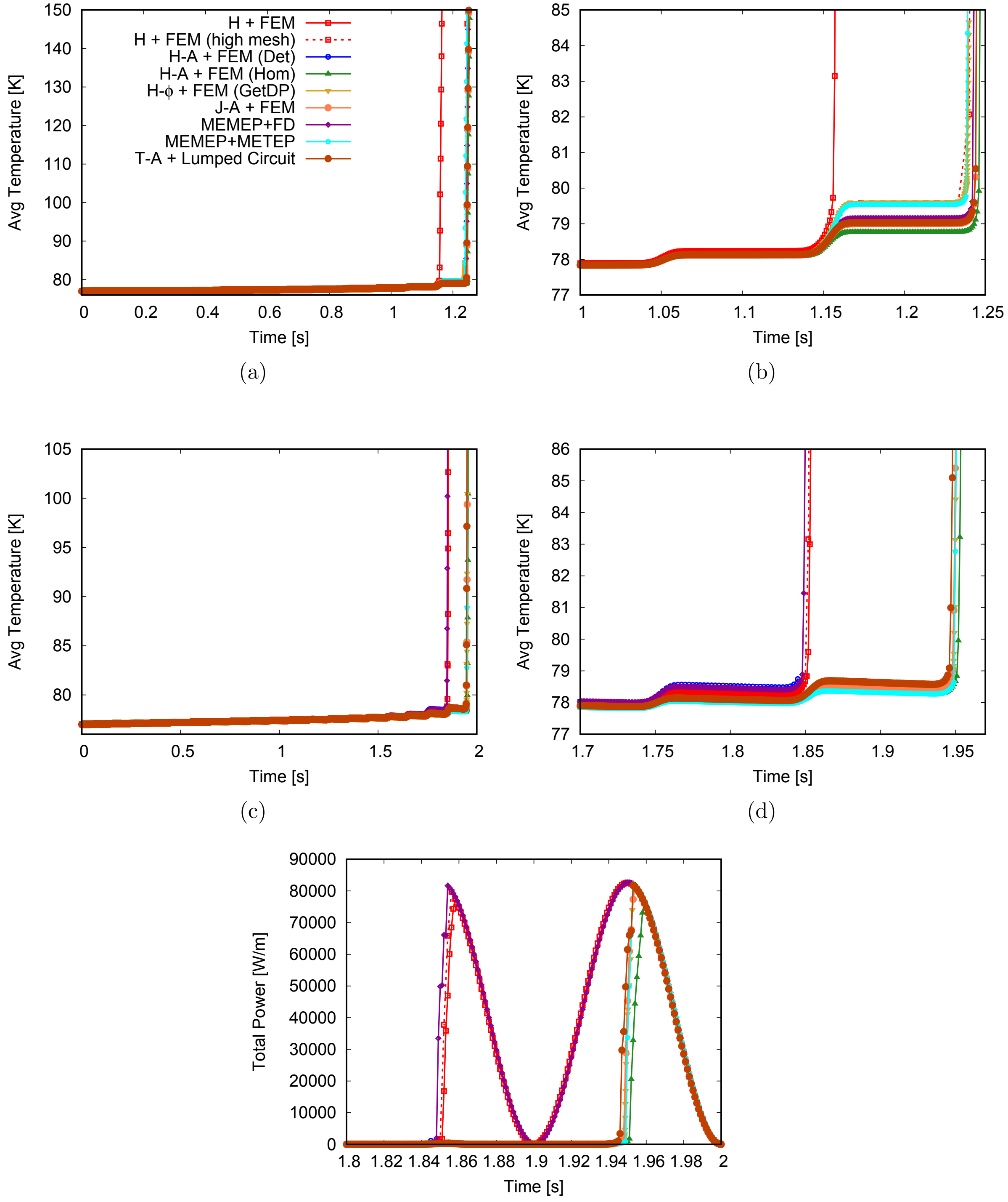

(a)

(b)

(c)

(d)

(e)

Figure 7: Comparison between homogenized models for racetrack coil at 180 A. Average temperatures are shown in (a) at adiabatic conditions, and in (c) with cooling conditions. (b,d) are zoomed versions of (a) and (b) respectively. The total power dissipation is shown in (e) at quench considering cooling conditions. All figures use the same legend as (a).

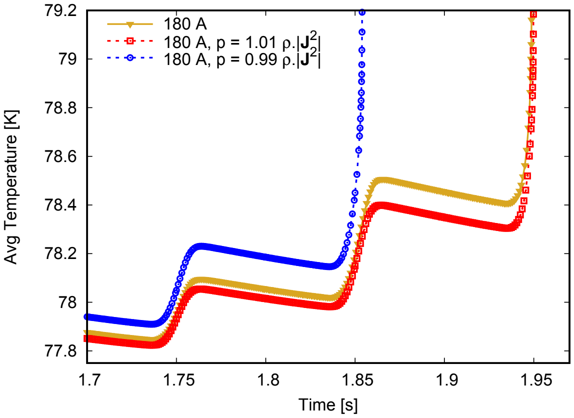

Figure 8: The change in average temperature when considering a 1 percent relative difference in local power loss density p is shown. These results are calculated with $\mathbf{H}$-ϕ + FEM model for 180 A current input with cooling conditions.

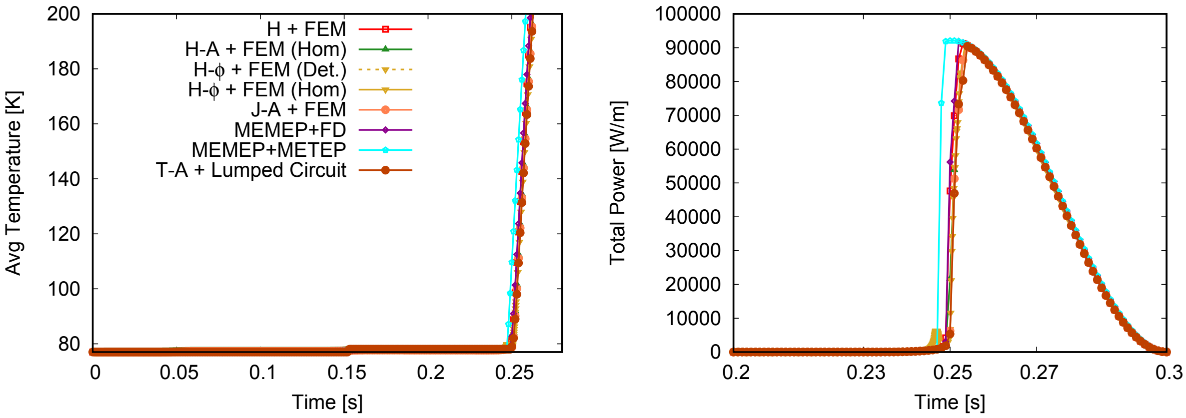

(a)

(b)

Figure 9: Comparison between homogenized models for racetrack coil at 190 A for (a) average temperature and (b) total power. All models show very good agreement at higher currents, and quench is reached at just 1.25th cycle. Both figures use the same legend.

half-cycle sooner when the local loss density is artificially increased by 1 percent with the $\mathbf{H}$-ϕ + FEM combination.

Although minor differences can be observed till input currents of around 180 A, these differences vanish at higher currents. This can be seen in the case of 190 A in Figure 9, where all the homogenized models agree with each other, and also with the detailed models, where they all predict quench at around 0.25 s.

The computing times for the homogenized models range from 6 to 40 minutes, which is much faster than detailed model (around 2.5 hours), for 180 A input case with cooling. It can be noted that coupling of an electromagnetic formulation with a different thermal formulation can affect the runtime of a model drastically. For example, MEMEP+FD combination solves the 180 A case in 6 minutes, but when MEMEP is coupled with METEP, the computing time is increased to around 20 minutes. Thus, choosing a fast and effective thermal formulation is also essential for such computations. However, a proper comparison of computing times, between different formulations specified here for homogenized method, is not meaningful as they were run by different teams on different computers. Also, many of these models are still in development and not optimized for speed yet. In future, such a comparison is possible when these models are optimized for computing speed, as well as the models are run on the same computing system.

4.3. Benchmark of different models: Pancake coil

Figure 10 shows the quench prediction by the considered detailed and homogenized models for the pancake coil study. We have used the same standard mesh for this study as the previous section. Here, $\mathbf{H}$-ϕ formulation is applied to COMSOL software. The homogenization does not include stycast in electromagnetic formulation for $\mathbf{H}$-ϕ. For the thermal formulation coupled with $\mathbf{H}$-ϕ (FEM), we have compared both cases, i.e., with and without stycast in homogenization. MEMEP + FD and $\mathbf{H}$ + FEM combinations uses stycast in homogenization for both electromagnetic and thermal formulations.

As expected, the temperature rise is fast and sudden due to the fast ramp rate of the input current (1 A/s). It is also faster than the racetrack coils, where you do not see quench until 180 s at least, which is due to different time dependence of the current input and the shape of the coil. This rise in temperature could be faster if not for copper, which increases the heat capacity of a homogenized turn (Table 2). The inclusion of copper here also increases the thermal conductivity in the axial direction (k_y) by up to 4 times as compared to the racetrack coil.

For the adiabatic case (Figure 10 (a)), we see perfect agreement between detailed model and homogenized models (with and without stycast). For the case with cooling, we see good agreement in all these models (Figure 10 (b,c)), specially till 160 A. We see a small temperature rise up to 160 A (Figure 10 (b)), and the quench is delayed by at least 6 s due to the cooling conditions (Figure 10 (c)). Here, the detailed model diverges above critical temperature, and the calculation is stopped automatically for that case. The homogenized models predict thermal runaway slightly earlier for these cases, as compared to the detailed model. However, this earlier estimation is not necessarily disadvantageous, since it suggests slightly stricter quench protection systems than required.

5. Conclusion

In this study, both detailed and homogenized electromagnetic-thermal models of HTS tapes have been applied to simulate the quench apparition in racetrack and pancake coils. Firstly, we show that the results obtained using the detailed and the homogenized

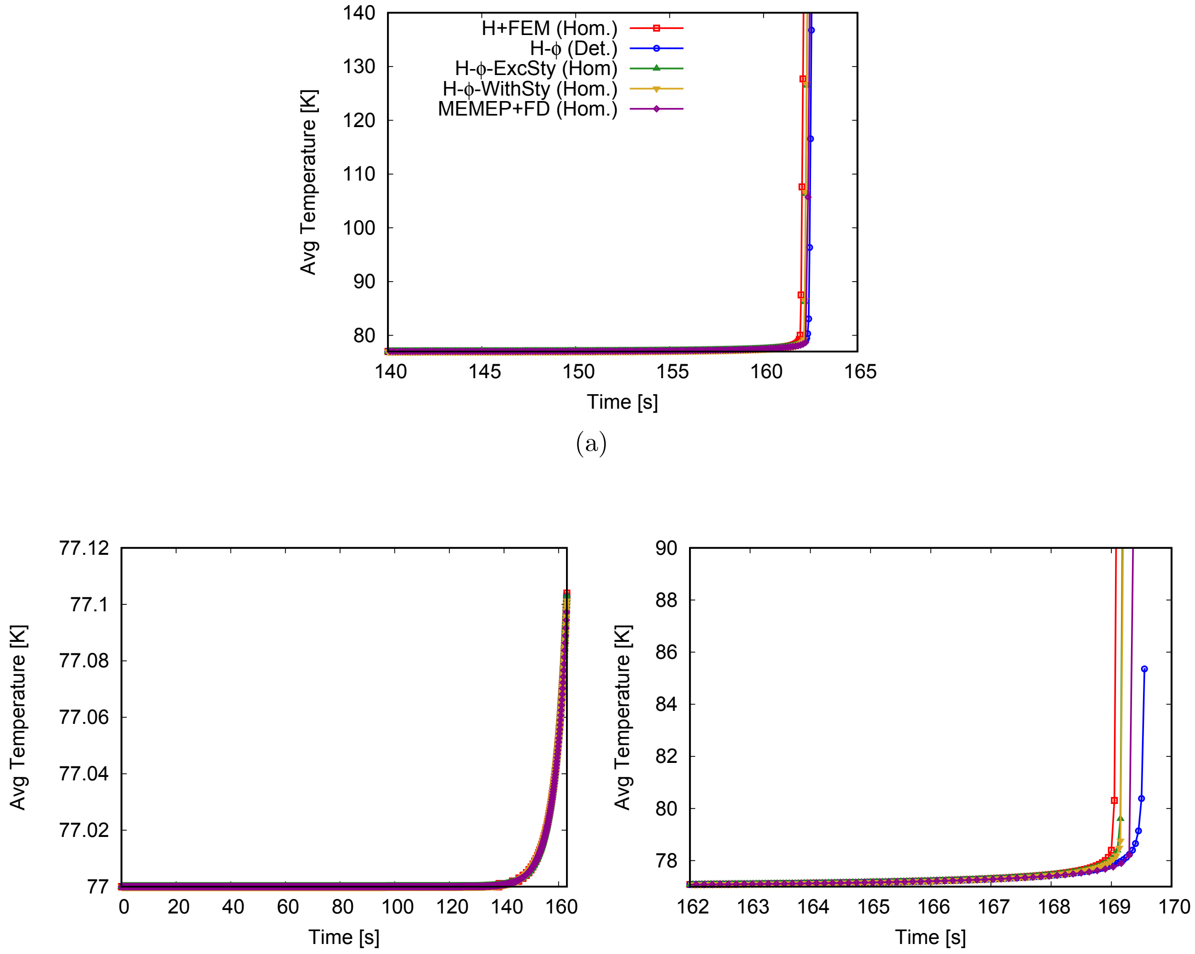

(a)

(b)

(c)

Figure 10: Comparison of average temperature for pancake coil is shown in (a) adiabatic conditions, and (b,c) cooling conditions. Good agreement is achieved between detailed model and homogenized models. All figures use the same legend as (a).

models only differ in the minimum temperature estimation, which is irrelevant for quench prediction. We also demonstrate that keeping the turn-to-turn insulation layers out of the homogenization procedure, by explicitly discretizing the stycast layers, can avoid this overestimation of the minimum temperature. Furthermore, we illustrate good agreements between the different homogenized and detailed models, as the several models developed by various research teams yield similar predictions in the terms of temperature rise and dissipated power. Moreover, we present the crucial impact of the accuracy of the electromagnetic submodel itself, as even a 1 percent relative difference in power dissipation can significantly impact the predicted instant of quench occurrence. The racetrack and pancake coils models proposed in this work can be considered as benchmarks for the HTS modeling community, and can be used for quick multiphysics analysis of REBCO coils (up to the onset of quench transitions) for various large-scale applications. Future experimental measurements may be conducted to validate the models proposed in this study, and models may be further developed to analyze temperatures during the thermal runaways.

6. Acknowledgements

This publication is partially based upon the work from COST Action CA19108, supported by COST (European Cooperation in Science and Technology). L. Denis is a research fellow funded by the F.R.S-FNRS.

7. References

[1] S. Hahn, K. Kim, K. Kim, X. Hu, T. Painter, I. Dixon, S. Kim, K. Bhattarai, S. Noguchi, J. Jaroszynski, and D.C. Larbalestier. 45.5-tesla direct-current magnetic field generated with a high-temperature superconducting magnet. *Nature*, 570(7762):496–499, 2019.

[2] S. Awaji, K. Watanabe, H. Oguro, S. Hanai, H. Miyazaki, M. Takahashi, S. Ioka, M. Sugimoto, H. Tsubouchi, S. Fujita, et al. New 25 T cryogen-free superconducting magnet project at Tohoku university. *IEEE transactions on applied superconductivity*, 24(3):1–5, 2013.

[3] Q. Wang, J. Liu, J. Zheng, J. Qin, Y. Ma, Q. Xu, D. Wang, W. Chen, T. Qu, X. Zhang, and D. Jiang. Progress of ultra-high-field superconducting magnets in China. *Superconductor Science and Technology*, 35(2):023001, 2021.

[4] LNCMI, France. SuperEMFL - Superconducting magnets for the European Magnet Field Laboratory. *H2020 Project*, 2021. `https://emfl.eu/superemfl/project`.

[5] C.C. Chow, M. D. Ainslie, and K.T. Chau. High temperature superconducting rotating electrical machines: An overview. *Energy Reports*, 9:1124–1156, 2023.

[6] K.S. Haran, S. Kalsi, T. Arndt, H. Karmaker, R. Badcock, B. Buckley, T. Haugan, M. Izumi, D. Loder, J.W. Bray, P. Masson, and E.W. Stautner. High power density superconducting rotating machines-Development status and technology roadmap. *Supercond. Sci. Technol.*, 30(12):123002, 2017.

[7] F. Grilli, T. Benkel, J. Hänisch, M. Lao, T. Reis, E. Berberich, S. Wolfstädter, C. Schneider, P. Miller, C. Palmer, B. Glowacki, V. Climente-Alarcon, A. Smara, L. Tomkow, J. Teigelkötter, A. Stock, J. Büdel, L. Jeunesse, M. Staempflin, G. Delautre, B. Zimmermann, R. van der Woude, A. Perez, S. Samoilenkov, A. Molodyk, E. Pardo, M. Kapolka, S. Li, and A. Dadhich. Superconducting motors for aircraft propulsion: the Advanced Superconducting Motor Experimental Demonstrator project. *Journal of Physics: Conference Series*, 1590(1):012051, 2020.

[8] G. G. Sotelo, F. Sass, M. Carrera, J. Lopez-Lopez, and X. Granados. Proposal of a novel design for linear superconducting motor using 2G tape stacks. *IEEE Transactions on Industrial Electronics*, 65(9):7477–7484, 2018.

[9] D.A. Cardwell, D.C. Larbalestier, and A. Braginski. *Handbook of Superconductivity: Characterization and Applications*, volume 3. CRC Press, 2021. `https://doi.org/10.1201/9781003139638`.

[10] A. Tollestrup and E. Todesco. The development of superconducting magnets for use in particle accelerators: From the tevatron to the LHC. *Reviews of Accelerator Science and Technology*, 1(01):185–210, 2008.

[11] L. Bottura, S. Prestemon, L. Rossi, and A. V. Zlobin. Superconducting magnets and technologies for future colliders. *Frontiers in Physics*, 10:935196, 2022.

[12] R. G. Sharma. *Superconducting Magnets in Fusion Reactors*, pages 483–547. Springer International Publishing, Cham, 2021.

[13] A. Badel, B. Rozier, B. Ramdane, G. Meunier, and P. Tixador. Modeling of 'quench' or the

occurrence and propagation of dissipative zones in REBCO high temperature superconducting coils. *Superconductor Science and Technology*, 32(9):094001, jul 2019.

[14] C. Jiaxiang, G. Mingzhi, T. Yujin, W. Xingzhe, and Z. Youhe. Quench detection and early warning based on thermoelastic strain rate for HTS tapes thermally triggered by heat spots. *Superconductor Science and Technology*, 36(1):015013, dec 2022.

[15] A. Vitrano, M. Wozniak, E. Schnaubelt, T. Mulder, E. Ravaioli, and A. Verweij. An open-source finite element quench simulation tool for superconducting magnets. *IEEE Transactions on Applied Superconductivity*, 33(5):1–6, 2023.

[16] E. Ravaioli, O. Tranum Arnegaard, A. Verweij, and M. Wozniak. Quench transient simulation in a self-protected magnet with a 3-D finite-difference scheme. *IEEE Transactions on Applied Superconductivity*, 32(6):1–5, 2022.

[17] M. Cho, S. Noguchi, J. Bang, J. Kim, U. Bong, J. T. Lee, S. B. An, K. R. Bhattarai, K. Kim, K. Kim, C. Im, K. J. Han, and S. Hahn. Combined circuit model to simulate post-quench behaviors of no-insulation HTS coil. *IEEE Transactions on Applied Superconductivity*, 29(5):1–5, 2019.

[18] A. Stenvall, T. Salmi, and E. Härö. *Introduction to Stability and Quench Protection*, chapter Chapter 2, pages 107–190.

[19] W. Hong, P. Miao, S. Hu, X. Zhang, H. Liu, and F. Liu. Two quenched models for high-temperature superconducting insulated coils. *IEEE Transactions on Applied Superconductivity*, 34(3):1–5, 2024.

[20] C. H. Bonnard, L. Frédéric Sirois, D. Christian, and G. Didier. Multi-scale model of resistive-type superconducting fault current limiters based on 2G HTS coated conductors. *Superconductor Science and Technology*, 30(1):014005, 2016.

[21] E. Pardo and A. Dadhich. Electro-thermal modelling by novel variational methods: Racetrack coil in short-circuit. *IEEE Transactions on Applied Superconductivity*, 33(5), 2023. 5201606.

[22] A. Dadhich, P. Fazilleau, and E. Pardo. A novel and coupled electromagnetic and electrothermal software for quench analysis of high field magnets. 2024. `https://arxiv.org/abs/2402.04034v2`.

[23] F. Roy, B. Dutoit, F. Grilli, and F. Sirois. Magneto-thermal modeling of second-generation HTS for resistive fault current limiter design purposes. *IEEE Transactions on Applied Superconductivity*, 18(1):29–35, 2008.

[24] K. Kajikawa, T. Hayashi, R. Yoshida, M. Iwakuma, and K. Funaki. Numerical Evaluation of AC Losses in HTS Wires With 2D FEM Formulated by Self Magnetic Field. *IEEE Transactions on Applied Superconductivity*, 13(2):3630–3633, 2003.

[25] R. Pecher, M.D. McCulloch, S. J. Chapman, L. Prigozhin, and C. M. Elliott. 3D-modelling of bulk type-II superconductors using unconstrained H-formulation. *Institute of Physics Conference Series*, 181, 2003.

[26] Z. Hong, A. M. Campbell, and T. A. Coombs. Numerical solution of critical state in superconductivity by finite element software. *Superconductor Science and Technology*, 19(12):1246–1252, 2006.

[27] R. Brambilla, F. Grilli, and L. Martini. Development of an edge-element model for AC loss computation of high-temperature superconductors. *Superconductor Science and Technology*, 20(1):16–24, 2007.

[28] B. Shen, F. Grilli, and T. Coombs. Overview of H-Formulation: A Versatile Tool for Modeling Electromagnetics in High-Temperature Superconductor Applications. *IEEE Access*, 8:100403–100414, 2020.

[29] E. Pardo and F. Grilli. Electromagnetic modeling of superconductors. *In: Numerical Modeling of Superconducting Applications*, pages 1–105, 2023. World Scientific Publishing Co Pte Ltd, `www.worldscientific.com/doi/10.1142/9789811271441_0001`.

[30] L. Bortot, B. Auchmann, I. C. Garcia, H. D. Gersem, M. Maciejewski, M. Mentink, S. Schöps, J. V. Nugteren, and A. P. Verweij. A coupled A–H formulation for magneto-thermal transients in

high-temperature superconducting magnets. *IEEE Transactions on Applied Superconductivity*, 30(5):1–11, 2020.

[31] F. Sirois and F. Grilli and A. Morandi. Comparison of constitutive laws for modeling high-temperature superconductors. *IEEE Transactions on Applied Superconductivity*, 29(1):1–10, 2019.

[32] J. Dular, C. Geuzaine, and B. Vanderheyden. Finite-element formulations for systems with high-temperature superconductors. *IEEE Transactions on Applied Superconductivity*, 30(3), 2020. 8200113.

[33] J. Dular. *Standard and Mixed Finite Element Formulations for Systems with Type-II Superconductors*. PhD thesis, University of Liege, Belgium, 2023.

[34] M. S. Pellikka, L. Suuriniemi Kettunen, and C. Geuzaine. Homology and cohomology computation in finite element modeling. *SIAM J. Sci. Comput.*, 35(5):B1195–B1214, 2013.

[35] C. Geuzaine and J.-F. Remacle. Gmsh: a three-dimensional finite element mesh generator with built-in pre- and post-processing facilities. *International Journal for Numerical Methods in Engineering*, 79(11):1309–1331, 2009.

[36] P. Dular, C. Geuzaine, F. Henrotte, and W. Legros. A general environment for the treatment of discrete problems and its application to the finite element method. *IEEE Transactions on Magnetics*, 34(5):3395–3398, 1998.

[37] Life-HTS. https://www.life-hts.uliege.be. Online; accessed on 02/05/2024.

[38] A. Arsenault, B. S. Alves, and F. Sirois. Comsol implementation of the H-ϕ-formulation with thin cuts for modeling superconductors with transport currents. *IEEE Transactions on Applied Superconductivity*, 31(6):1–9, 2021.

[39] HTS modelling workgroup. Modelling of high temperature superconductors (HTS). 2024. `https:\.htsmodelling.com`.

[40] G. dos Santos, B. M. O. Santos, S. Felipe, G. R. M. Flávio, G. S. Guilherme, and J. A. Rubens. J-A formulation: A finite element methodology for simulating superconducting devices. *Superconductivity*, 6:100049, 2023.

[41] B. M. O. Santos, G. dos Santos, F. G. dos Reis Martins, F. Sass, G. G. Sotelo, and R. de Andrade. Use of the J-A approach to model homogenized 2G tape stacks and hts bulks. *IEEE Transactions on Applied Superconductivity*, 34(3):1–5, 2024.

[42] B. M. O. Santos, G. dos Santos, N. G. Santos, and R. J. Rubens. J-A approach to simulations of hts tapes: How to couple with electric circuits. *IEEE Transactions on Applied Superconductivity*, 34(4):1–4, 2024.

[43] G. dos Santos and B. M. O. Santos. Enhancing electric field calculation in HTS tape simulations for currents exceeding the critical limit using full hts tape modeling. *Physica C: Superconductivity and its Applications*, 622:1354518, July 2024.

[44] G. Santos, F. Trillaud, B. M. O. Santos, F. Sass, and G. G. Sotelo. Fast coupled thermoelectric and magnetic model to simulate the transient behavior of inductive and resistive superconducting fault-current limiters. *IEEE Transactions on Applied Superconductivity*, 34(1):1–17, 2024.

[45] G. Santos, B. M. O. Santos, F. G. R. Martins, F. Sass, G. G. Sotelo, and R. Andrade. An integrated methodology to assess AC losses in the kHz range using the FEM and partial element equivalent circuit. *IEEE Transactions on Applied Superconductivity*, 32(2):1–8, 2022.

[46] W. Durante-Gómez, F. Trillaud, G. dos Santos, F. Gonzalez-Montañez, G. Hajiri, K. Berger, and J. de la Cruz-Soto. FEM-circuit co-simulation of superconducting synchronous wind generators connected to a DC network using the homogenized J–A formulation of the maxwell equations. *Superconductor Science and Technology*, 37(6):065021, May 2024.

[47] E. Pardo, J. Šouc, and L. Frolek. Electromagnetic modelling of superconductors with a smooth current-voltage relation: variational principle and coils from a few turns to large magnets. *Supercond. Sci. Technol.*, 28:044003, 2015.

[48] E. Pardo. Modeling of screening currents in coated conductor magnets containing up to 40000 turns. *Supercond. Sci. Technol.*, 29(8):085004, 2016.

[49] E. Pardo and M. Kapolka. 3D computation of non-linear eddy currents: Variational method and superconducting cubic bulk. *Journal of Computational Physics*, 344:339–363, 2017.

[50] H. Zhang, M. Zhang, and W. Yuan. An efficient 3D finite element method model based on the T–A formulation for superconducting coated conductors. *Superconductor Science and Technology*, 30(2):024005, dec 2016.

[51] F. Huber, W. Song, M. Zhang, and F. Grilli. The T-A formulation: an efficient approach to model the macroscopic electromagnetic behaviour of hts coated conductor applications. *Superconductor Science and Technology*, 35(4):043003, mar 2022.

[52] E. Berrospe-Juarez, V. M. R. Zermeño, F. Trillaud, and F. Grilli. Real-time simulation of large-scale HTS systems: multi-scale and homogeneous models using the T–A formulation. *Superconductor Science and Technology*, 32(6):065003, apr 2019.

[53] R. Wrobel and P. H. Mellor. A general cuboidal element for three-dimensional thermal modelling. *IEEE Transactions on Magnetics*, 46(8):3197–3200, 2010.

[54] J. Nerg, M. Rilla, and J. Pyrhonen. Thermal analysis of radial-flux electrical machines with a high power density. *IEEE Transactions on Industrial Electronics*, 55(10):3543–3554, 2008.